Geoscience Frontiers xxx (2018) 1–12

HOSTED BY

ELSEVIER

Contents lists available at ScienceDirect

China University of Geosciences (Beijing)

Geoscience Frontiers

journal homepage: www.elsevier.com/locate/gsf

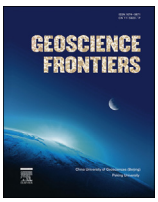

Timescales of interface-coupled dissolution-precipitation reactions on carbonates

François Renard [a,b,*], Anja Røyne [a], Christine V. Putnis [c,d]

[a] The Njord Centre, Physics of Geological Processes, Departments of Geoscience and Physics, University of Oslo, Norway
[b] Univ. Grenoble Alpes, Univ. Savoie Mont Blanc, CNRS, IRD, IFSTTAR, ISTerre, 38000, Grenoble, France
[c] Institut für Mineralogie, University of Münster, Corrensstrasse 24, 48149, Münster, Germany
[d] The Institute for Geoscience Research (TIGeR), Department of Chemistry, Curtin University, Perth, 6845, Australia

ARTICLE INFO

Article history:
Received 20 November 2017
Received in revised form
1 February 2018
Accepted 27 February 2018
Available online xxx

Keywords:
Carbonates
Atomic force microscopy
Dissolution
Precipitation
Boundary layer
Replacement

ABSTRACT

In the Earth's upper crust, where aqueous fluids can circulate freely, most mineral transformations are controlled by the coupling between the dissolution of a mineral that releases chemical species into the fluid and precipitation of new minerals that contain some of the released species in their crystal structure, the coupled process being driven by a reduction of the total free-energy of the system. Such coupled dissolution-precipitation processes occur at the fluid-mineral interface where the chemical gradients are highest and heterogeneous nucleation can be promoted, therefore controlling the growth kinetics of the new minerals. Time-lapse nanoscale imaging using Atomic Force Microscopy (AFM) can monitor the whole coupled process under *in situ* conditions and allow identifying the time scales involved and the controlling parameters. We have performed a series of experiments on carbonate minerals (calcite, siderite, dolomite and magnesite) where dissolution of the carbonate and precipitation of a new mineral was imaged and followed through time. In the presence of various species in the reacting fluid (e. g. antimony, selenium, arsenic, phosphate), the calcium released during calcite dissolution binds with these species to form new minerals that sequester these hazardous species in the form of a stable solid phase. For siderite, the coupling involves the release of Fe^{2+} ions that subsequently become oxidized and then precipitate in the form of Fe^{III} oxyhydroxides. For dolomite and magnesite, dissolution in the presence of pure water (undersaturated with any possible phase) results in the immediate precipitation of hydrated Mg-carbonate phases. In all these systems, dissolution and precipitation are coupled and occur directly in a boundary layer at the carbonate surface. Scaling arguments demonstrate that the thickness of this boundary layer is controlled by the rate of carbonate dissolution, the equilibrium concentration of the precipitates and the kinetics of diffusion of species in a boundary layer. From these parameters a characteristic time scale and a characteristic length scale of the boundary layer can be derived. This boundary layer grows with time and never reaches a steady state thickness as long as dissolution of the carbonate is faster than precipitation of the new mineral. At ambient temperature, the surface reactions of these dissolving carbonates occur on time-scales of the order of seconds to minutes, indicating the rapid surface rearrangement of carbonates in the presence of aqueous fluids. As a consequence, many carbonate-fluid reactions in low temperature environments are controlled by local thermodynamic equilibria rather than by the global equilibrium in the whole system.

1. Introduction

In fluid-rock interactions, many processes are coupled; for example the dissolution of one mineral may provide chemical species resulting in supersaturation with respect to another mineral, with a lower free energy, that then precipitates (Putnis, 2009; Ruiz-Agudo et al., 2014). Among minerals, carbonates are very

* Corresponding author. The Njord Centre, Physics of Geological Processes, Departments of Geoscience and Physics, University of Oslo, Norway.
E-mail address: francois.renard@geo.uio.no (F. Renard).
Peer-review under responsibility of China University of Geosciences (Beijing).

https://doi.org/10.1016/j.gsf.2018.02.013

common in the Earth's upper crust and because of their high reactivity they dissolve and precipitate easily (Morse and Arvidson, 2002), thus playing a key role in the global cycle of carbon, as well as other elements incorporated in the carbonate structure (such as Mg). They are present at the surface of Mars and their reactivity controls weathering at the surface of this planet (Phillips-Lander et al., 2017). On Earth, carbonates control the weathering of continents and the formation of sediments in oceans and lakes and they buffer the composition of groundwaters through pH, alkalinity or metal concentrations (Morse et al., 2007). Moreover, they can interact with pollutants and immobilize them. For example, when considering calcite, several cations (Paquette and Reeder, 1995; Rimstidt et al., 1998; Davis et al., 2000; Stipp et al., 2006) and anions (Dove and Hochella, 1993; Alexandratos et al., 2007; Montes-Hernandez et al., 2009) can be incorporated or interact with the mineral surfaces, making calcite a potential sink for these elements at the global scale. A lot of research has centered on carbonate dissolution kinetics (Pokrovsky et al., 2009 and references therein) but coupled reactions are less well studied.

Fluid-rock interface-coupled dissolution-precipitation reactions that involve carbonates (Ruiz-Agudo and Putnis, 2012; Ruiz-Agudo et al., 2014) can be observed *in situ* and at the nanoscale by using atomic force microscopy, AFM (Fig. 1a). The entire process is controlled by the surface of the dissolving mineral where chemical potential gradients are the highest during dissolution and by a boundary layer that becomes supersaturated with respect to the precipitating mineral (Fig. 1b). Two important effects play a role in such processes: variations of fluid composition and pH near the mineral surface during dissolution have been reported using phase-shift interferometry (Ruiz-Agudo et al., 2016); and the nanoscale rates of dissolution at a mineral surface are spatially heterogeneous and can vary by orders of magnitude (Dove and Platt, 1996; Arvidson et al., 2003; Fischer et al., 2012, 2014; Briese et al., 2017). Based on properties of the surface chemistry of calcite, backed up by supporting AFM imaging of the nucleated phases, we quantify here processes of dissolution, nucleation, and precipitation at carbonate surfaces using data acquired in previous studies (Urosevic et al., 2012; King and Putnis, 2013; Klasa et al., 2013; Putnis et al., 2013; Renard et al., 2015, 2017, 2018).

In these systems, the coupled dissolution of the carbonate mineral and the heterogeneous nucleation of a precipitate occur at the surface of the dissolving mineral, with either crystallographic control (epitaxial growth) or thermodynamic control (supersaturation will be highest at dissolution sites). This interface-coupled process may control the mobilization and localization of several inorganic pollutants in natural environments such as selenium, arsenic or antimony. It also provides a new mechanism for trapping and effectively sequestering them on carbonates (Montes-Hernandez et al., 2009; Putnis et al., 2013; Renard et al., 2015, 2018). More generally, such direct observations show that fluid-

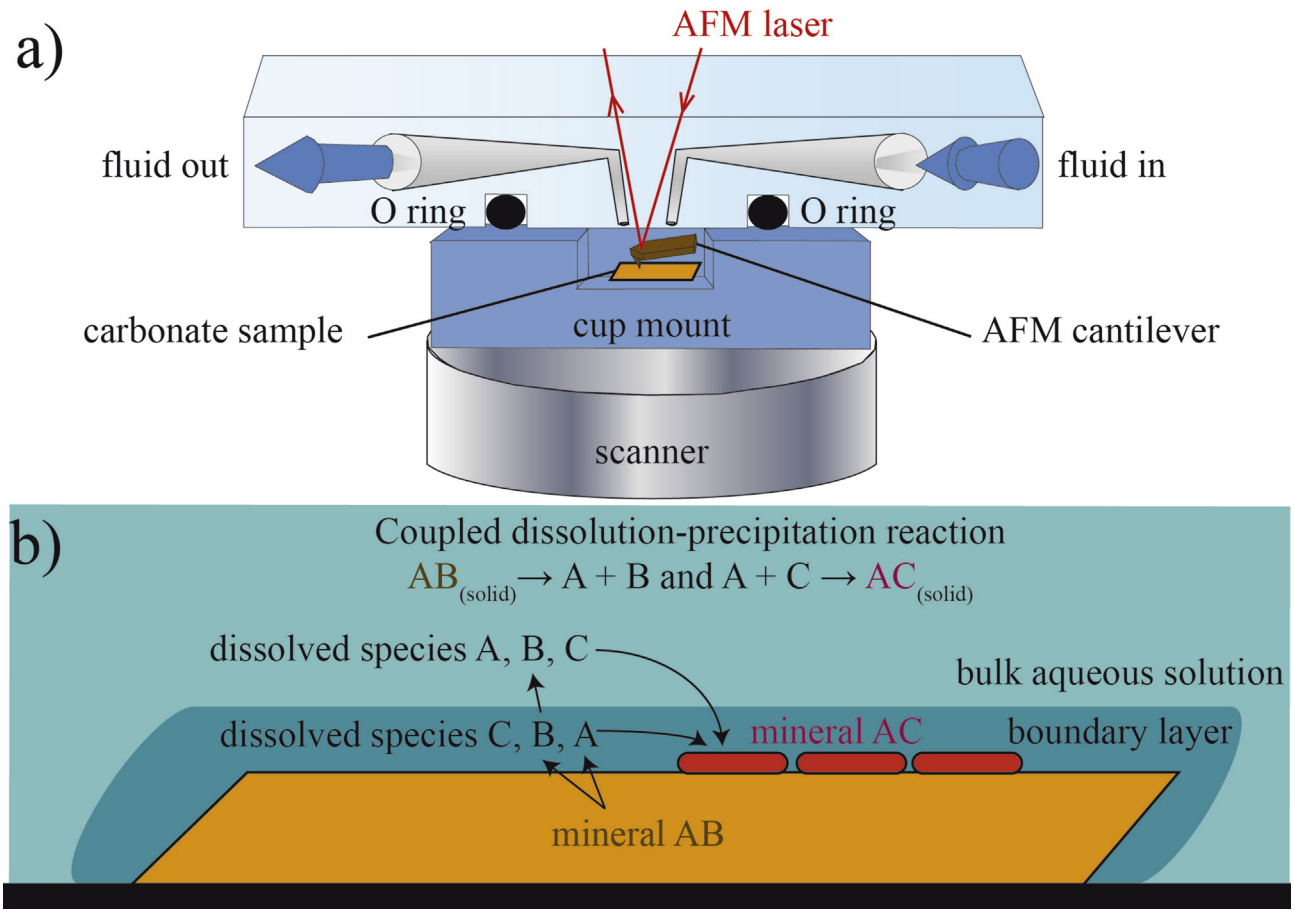

Figure 1. Concept of the interface-coupled dissolution-precipitation process. (a) Sketch of the apparatus used for nanoscale *in situ* imaging of fluid rock interactions. The carbonate sample (approx. 3 mm × 2 mm × 1 mm) is fixed inside a flow-through fluid-cell (volume 50 μL) coupled to an atomic force microscope, allowing *in situ* time-lapse imaging of the reacting surface. Image modified per favour of J. M. Astilleros at Madrid Complutense University, Spain. (b) Concept of coupled dissolution precipitation. Here AB is a carbonate mineral that dissolves, where A is the cation that can bind with the species C to reach supersaturation allowing for precipitation of the new mineral AC. The reaction occurs in a boundary layer where the speciation and thermodynamic equilibrium differs from the bulk fluid.

Please cite this article in press as: Renard, F., et al., Timescales of interface-coupled dissolution-precipitation reactions on carbonates, Geoscience Frontiers (2018), https://doi.org/10.1016/j.gsf.2018.02.013

rock reactions can be controlled by mechanisms occurring in a fluid boundary layer at the mineral surface with a different chemistry to the bulk fluid (Ruiz-Agudo et al., 2016), confirming the crucial role of the mineral-water interface, where reactions between minerals and their environment take place (Putnis and Ruiz-Agudo, 2013).

Here, we study these coupled dissolution-precipitation processes at various carbonate interfaces where the entire process is controlled by a boundary layer whose thickness depends on the thermodynamic and kinetic parameters of the system. We exclude more complex replacement reactions, i.e. with generation of porosity (Putnis, 2002) and the presence of a mechanical boundary layer when a turbulent flow is imposed at some distance above the mineral surface (Liu and Deybrodt, 1997, 2001). This article is organized in the following way: First we describe a series of experiments where carbonate dissolution is coupled to the precipitation of a new mineral and the process is observed *in situ* with time-lapse imaging at the nanoscale using AFM. We observe the formation of precipitates in all of these systems, and in most cases their growth rate can be measured. Next, we use simple scaling arguments to discuss the existence of the boundary layer and how its thickness is controlled by the measured rate of carbonate dissolution, the measured rate of precipitate growth, the sizes of dissolution sites and precipitates, and the rate of diffusion of dissolved species in water.

2. Material and methods

All experiments were performed under conditions where we observed the existence of coupled dissolution-precipitation processes at the mineral surface, allowing the simultaneous measurement of carbonate dissolution and precipitation of a new phase. *In-situ* AFM images are acquired in seven systems: arsenic-calcite, selenium-calcite, antimony-calcite, phosphate-calcite, iron oxyhydroxide-siderite, dolomite and magnesite (Table 1). The experimental protocols are detailed in previous studies (Urosevic et al., 2012; King and Putnis, 2013; Putnis et al., 2013, 2014; Renard et al., 2015, 2017, 2018) and we summarize the main points below. The carbonate surfaces are scanned *in situ* during reaction at room temperature (22 ± 1 °C) using a Bruker Multimode AFM operating in contact mode. All time-resolved sequences were

Table 1
List of experiments. IS: ionic strength; pH: measured before injection.

Exp.#	Carbonate	Solution	Observations
Se13	Calcite	200 ppm $Se^{(IV)}$ pH = 9.1 IS = 7.6×10^{-3}	Many precipitates ($CaSeO_3 \cdot H_2O$) cover the surface. v_{sum} in the range 2.1–4.2 nm s^{-1}.
Se15	Calcite	200 ppm $Se^{(IV)}$ pH = 9.1 IS = 7.6×10^{-3}	Many precipitates ($CaSeO_3 \cdot H_2O$) grow in etch pits and near steps. v_{sum} in the range 2.1–4.2 nm s^{-1}.
Se17	Calcite	70 ppm $Se^{(IV)}$ pH = 8.5 IS = 2.6×10^{-3}	Many precipitates ($CaSeO_3 \cdot H_2O$) nucleate on the obtuse angle of the etch pits. Large precipitates form after one hour and cover the whole surface. v_{sum} in the range 2.1–4.2 nm s^{-1}.
Sb-Ca1	Calcite	200 ppm, $Sb^{(V)}$ pH = 3 IS = 5×10^{-2}	Many precipitates ($Ca_2Sb_2O_7$) nucleate and cover the surface. v_{sum} too large, cannot be measured.
Sb-Ca2	Calcite	200 ppm, $Sb^{(V)}$ pH = 5.1 IS = 5×10^{-2}	Many precipitates ($Ca_2Sb_2O_7$) nucleate and cover the surface. v_{sum} in the range 2.6 ± 1.3 to 4.1 ± 0.5 nm s^{-1}.
Sb-Ca4	Calcite	200 ppm, $Sb^{(V)}$ pH = 3.7 IS = 5×10^{-2}	Many precipitates ($Ca_2Sb_2O_7$) nucleate and cover the surface. v_{sum} too large, cannot be measured.
Sb-Ca6	Calcite	200 ppm, $Sb^{(V)}$ pH = 2.5 IS = 5×10^{-2}	Many precipitates ($Ca_2Sb_2O_7$) nucleate and cover the surface. v_{sum} too large, cannot be measured.
Sb-Ca9	Calcite	10 ppm, $Sb^{(V)}$ pH = 3 IS = 5×10^{-2}	Many precipitates ($Ca_2Sb_2O_7$) nucleate and cover the surface. v_{sum} too large, cannot be measured.
As-d-01	Calcite	500 ppm $As^{(V)}$ pH = 11.1 IS = 1.6×10^{-2}	Formation of precipitates (Ca-arsenate phases such as pharmacolite ($CaHAsO_4 \cdot 2H_2O$) and johnbaumite ($Ca_5(AsO_4)_3OH$)). v_{sum} = 1.9 ± 0.1 nm s^{-1}, up to 10 nm s^{-1}.
As-d-02	Calcite	500 ppm $As^{(V)}$ pH = 11.2 IS = 1.6×10^{-2}	Formation of precipitates (Ca-arsenate phases such as pharmacolite ($CaHAsO_4 \cdot 2H_2O$) and johnbaumite ($Ca_5(AsO_4)_3OH$)). v_{sum} = 2.5 ± 0.4 nm s^{-1}, up to 10 nm s^{-1}.
As-d-03	Calcite	500 ppm $As^{(V)}$ pH = 11.2 IS = 4.7×10^{-2}	Formation of precipitates (Ca-arsenate phases such as pharmacolite ($CaHAsO_4 \cdot 2H_2O$) and johnbaumite ($Ca_5(AsO_4)_3OH$)). v_{sum} = 1.5 ± 0.2 nm s^{-1}, up to 10 nm s^{-1}.
Sid11	Siderite	pH = 1.6 IS = 4.7×10^{-2}	More than 80% of the original surface is covered by precipitates (likely goethite and/or ferrihydrite) after 17 h.
Sid15	Siderite	pH = 1 IS = 4.7×10^{-2}	More than 80% of the original surface is covered by precipitates (likely goethite and/or ferrihydrite) after 8.7 h v_{sum} = 0.14 ± 0.05 nm s^{-1} for the spreading of etch pits at pH 1.
Sid16	Siderite	pH = 1 IS = 4.7×10^{-2}	More than 80% of the original surface is covered by precipitates (likely goethite and/or ferrihydrite) after 1 h v_{sum} = 0.14 ± 0.05 nm s^{-1} for the spreading of etch pits at pH 1.
Magnesite8 Magnesite11	Magnesite	0.5 M Na_2SO_4 pH 2	Initial precipitates observed within several minutes and several larger precipitates after 12 h (likely hydrated magnesite phases such as nesquehonite and artinite). v_+ = 0.016 ± 0.002 nm s^{-1} for the spreading of etch pits at pH 2.
Dolomite8 Dolomite30	Dolomite	pH 3 IS = 2×10^{-3}	Precipitates cover 80% of the surface after 30 min (likely hydrated magnesite phases such as nesquehonite, hydromagnesite, and landfordite). v_{sum} = 0.088 ± 0.001 nm s^{-1} for the spreading of etch pits at pH 3.
Calcite6 Calcite7	Calcite	pH 8 50 mM $(HN_4)_2HPO_4$	Precipitates of calcium phosphate form as nm size particles that merge and form 2D chains and eventually cover the calcite surface – within 12 h. Initial precipitates are amorphous and crystallize into apatite within a few days.

Please cite this article in press as: Renard, F., et al., Timescales of interface-coupled dissolution-precipitation reactions on carbonates, Geoscience Frontiers (2018), https://doi.org/10.1016/j.gsf.2018.02.013

acquired downscan. The experiments were performed within an O-ring sealed flow-through fluid cell from Digital Instruments (Fig. 1a). At regular time intervals between each scan (each scan lasting 1.5 min), 2 mL of fluid was injected with a syringe, giving an effective flow rate of 22 $\mu L\ s^{-1}$. Prior test experiments using gravity feed continuous flow with constant solution height were made to confirm the observations. However, the quality of the AFM images was lower because the continuous flow that interacted with the AFM tip producing unwanted interference. Therefore, all experiments of the present study are performed with intermittent injections every 1.5 min. AFM images were collected using Si_3N_4 tips (Veeco Instruments, tip model NP-S20) with spring constants 0.12 N m^{-1} and 0.58 N m^{-1}. Images were analyzed using the NanoScope software (Version 5.31r1).

The optically clear rhombohedral carbonate crystals were obtained from geological museums (Natural History Museum, London and the University of Münster; the Iceland Spar, $CaCO_3$ is from Chihuahua, Mexico) and ICP-OES (Inductively Coupled Plasma-Optical Emission Spectroscopy) analyses revealed their high purity, with only trace (ppb) amounts of other elements (for calcite, predominantly Mg). Rhombohedral fragments (ca. 4 mm × 2 mm × 1 mm) were cleaved directly before each experiment from these crystals, and surfaces parallel to the cleavage plane were imaged: {10−14} for calcite, $CaCO_3$, siderite, $FeCO_3$, magnesite, $MgCO_3$ and dolomite $CaMg(CO_3)_2$.

Two types of aqueous solutions were used in the dissolution experiments. Firstly, pure water solutions with controlled pH and ionic strength were injected into the flow-through fluid cell to dissolve the carbonate surface. These solutions were prepared using doubled deionized water (resistivity > 18 $m\Omega\ cm^{-1}$) directly before each experiment. Sodium chloride, hydrochloric acid, and sodium hydroxide stock solutions were used to adjust ionic strength and pH. The formation of crystallographically-controlled rhombohedral etch pits (Fig. 2) could be observed during this step. Measurements of step retreat velocity (or etch pit spreading rate) at the carbonate surface are made from sequential images scanned in the same direction. The retreat velocity v_{sum} (nm s^{-1}) given by $v_{sum} = (v_+ + v_-)$, where v_+ and v_- are the retreat velocities of + and − steps, respectively, are calculated measuring the length increase per unit time between opposite parallel steps in sequential images (see Paquette and Reeder (1995) for the nomenclature of etch pits). Next, solutions with a controlled concentration of a new species (such as antimony or selenium or arsenic oxyanions), with the same pH and ionic strength as the aqueous solutions initially used, were injected into the fluid cell (see Table 1). These solutions were prepared from salts dissolved in double deionized water. The pH and salinity were adjusted according to thermodynamic simulations using the PHREEQC software (Parkhurst and Appelo, 1999). The pH of the solutions was also measured independently using a pH-meter, confirming the PHREEQC simulation results. For three carbonates (siderite, dolomite and magnesite), only deionized water with controlled ionic strength and pH was injected, because the precipitates that form are composed of species from the original carbonate and water only.

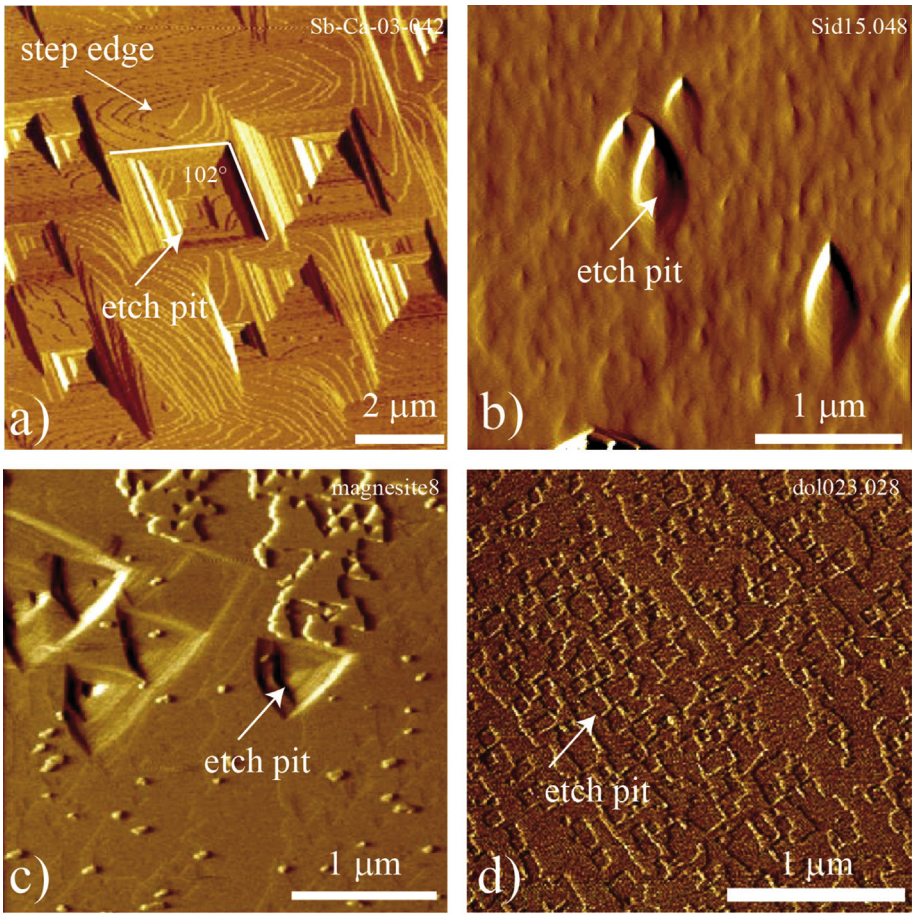

Figure 2. Representative AFM image of a carbonate surface during dissolution (deflection mode). (a) Topographic gradients on a calcite surface, underlining typical dissolution features such as step edges (height of one unit cell of calcite, 0.31 nm) and rhombohedral etch pits. The angle of 102° of the etch pit is that of the crystalline lattice in calcite (solution at pH 4). (b) Etch pit on a surface of siderite (solution at pH 1). (c) Etch pits on a surface of magnesite (solution at pH 2, after 12 h). (d) Etch pits on a surface of dolomite (pH 3).

Please cite this article in press as: Renard, F., et al., Timescales of interface-coupled dissolution-precipitation reactions on carbonates, Geoscience Frontiers (2018), https://doi.org/10.1016/j.gsf.2018.02.013

After several experiments, the carbonate sample was left in the solution to let the new precipitates grow over a period of 12–20 h. The carbonate surface covered with the precipitates was subsequently analyzed with Raman spectroscopy and scanning electron microscopy (SEM) to identify the precipitates, and to confirm that they are different from the salts used to prepare the interacting solutions.

3. Results

Several observations can be performed that are common to all experiments. The dissolution of carbonates occurs along step edges, kinks, and etch pits (Fig. 2), and precipitates form in all cases (Fig. 3, Table 1). These precipitates could be localized preferentially at specific sites (etch-pits, kinks) on the carbonate surface (Fig. 3a, c

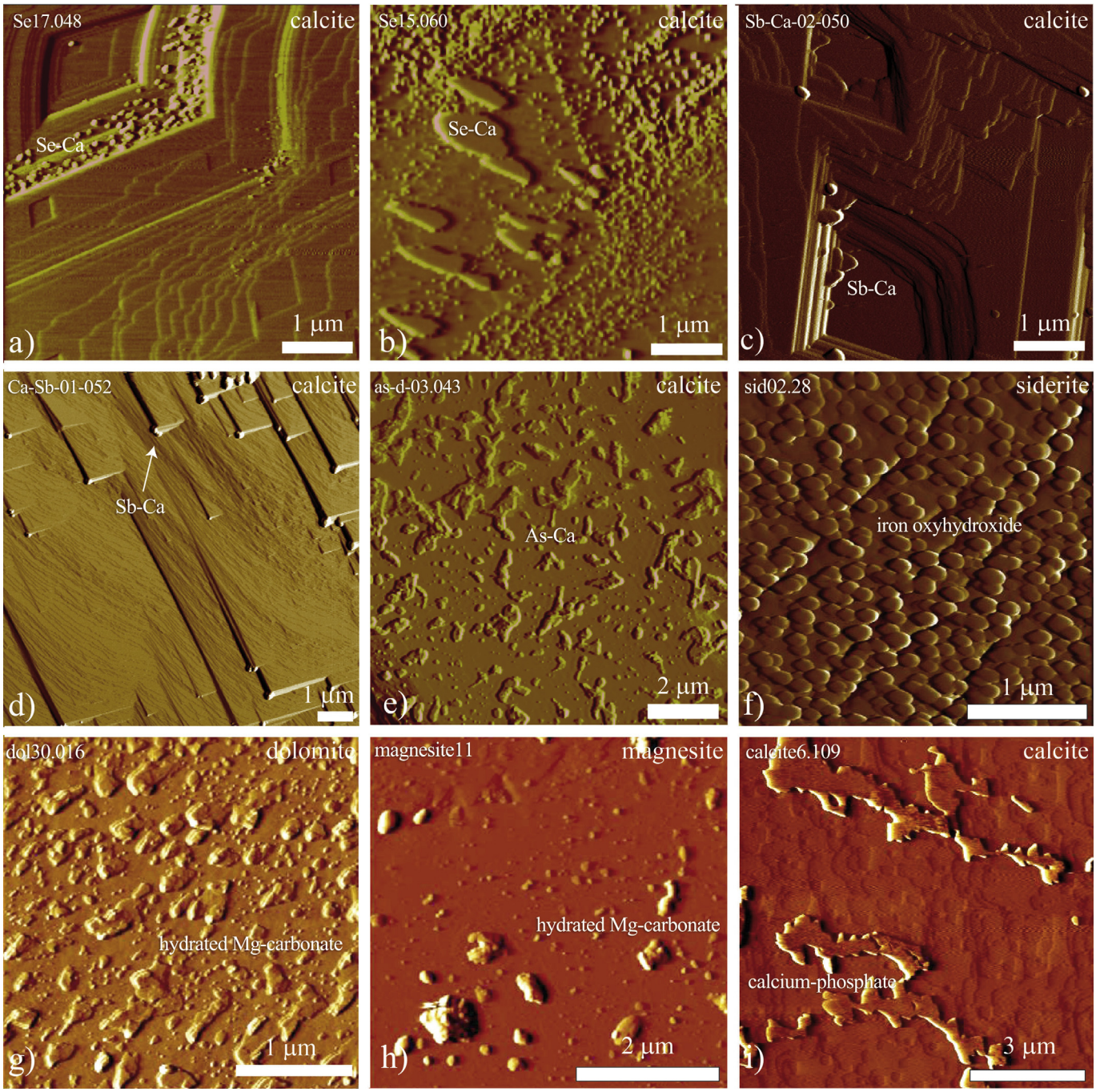

Figure 3. AFM deflection images of precipitates on carbonate surfaces. (a) Selenium-calcium phase. The newly formed precipitates are located inside a large etch pit. (b) Epitaxial growth of the selenium-calcium precipitate. (c and d) Antimony-calcium precipitates are located either inside etch pits or at kink sites over the calcite surface (white arrow). (e) Arsenic-calcium precipitate particles on a calcite surface. (f) Iron oxyhydroxide precipitates on a siderite surface. Here the coupled dissolution-precipitation reaction involves an additional step where the Fe^{2+}, released by siderite dissolution, is oxidized in the boundary layer before precipitating into the new mineral (hydrated Fe^{III} oxide/hydroxide phases). (g) Hydrated Mg-carbonate phase precipitated on dolomite (pH 3). (h) Hydrated magnesite phase precipitated on magnesite (pH 2). (i) Calcium phosphate phase precipitated on calcite (pH 7.9), see also Video S1.

Please cite this article in press as: Renard, F., et al., Timescales of interface-coupled dissolution-precipitation reactions on carbonates, Geoscience Frontiers (2018), https://doi.org/10.1016/j.gsf.2018.02.013

and d) and sometimes cover the entire surface after less than an hour (Fig. 3f). The adhesion of the new precipitates to the carbonate surface is initially weak, as revealed by the fact that some initial particles are moved by the tip of the AFM during scanning. After several minutes in all cases, adhesion to the substrate underneath is strong enough to avoid this effect. In several cases there is a control of the orientation of the precipitate (calcium-selenite, phosphates) by the calcite surface, where possible epitaxial growth of the precipitate on the calcite surface could be observed (Fig. 3b).

In all experiments, precipitates initially form thin flat disks or platelets that nucleate in a boundary layer above the carbonate surface or directly on the surface. Then, these precipitates are observed *in situ* to grow in height more or less linearly with time, while the diameter initially remains constant (Fig. 4). The imaging of initial particles is limited by the AFM capabilities but in general particles of only a few nanometers can be observed. These small particles then tend to grow and merge to form larger particle clusters. In several cases, the direct step retreat velocity in etch pits could be measured and falls in the range 1–5 nm s^{-1} for calcite in the pH range of 4–8 and 0.14 nm s^{-1} for siderite at pH 1 (Table 1). This direct measurement of a local dissolution rate on the carbonate surface is used below to estimate a rate of influx of cations in a boundary layer above the mineral surface (see Section 4). Observations specific to each fluid-carbonate system are discussed in the following.

Calcium-selenite precipitate and calcite. As soon as a selenium-bearing solutions with a fixed concentration of selenium $Se^{(IV)}$ oxyanions (Table 1) is introduced into the fluid cell, precipitates are immediately observed forming on the calcite surfaces (Putnis et al., 2013). The precipitate is identified as a hydrated calcium-selenite phase, likely $CaSeO_3 \cdot H_2O$ because it is the most stable phase in the present experimental conditions. The total reaction can be written as:

$$CaCO_3 + SeO_3^{2-} + H_2O \leftrightarrow CaSeO_3 \cdot H_2O + CO_3^{2-}$$

Nucleation starts immediately after the injection and the precipitates form while calcite is still dissolving. AFM images these particles at the calcite surface, but we cannot rule out that some particles formed initially in the boundary layer and then settled on the surface. Nucleation and precipitation occur predominantly along multiple step edges such as deep etch pits seen in Fig. 3a. These precipitates initiate as small particles on the calcite surface that slowly grow into platy forms up to 500 nm long (Fig. 3b), limited by well-defined straight edges. The heights of these islands range from a minimum of ca. 1.5 nm up to 14.5 nm after around one hour of reaction. The precipitates cover the whole scanned surface in less than one hour of continuous solution flow. The larger, flatter particles that form on the calcite surface appear oriented on the substrate and tend to elongate by adjacent particle attachment following specific directions (Fig. 3b), possibly implying some epitaxial crystallographic control on the nucleation and growth of the calcium selenite phase by the underlying calcite surface.

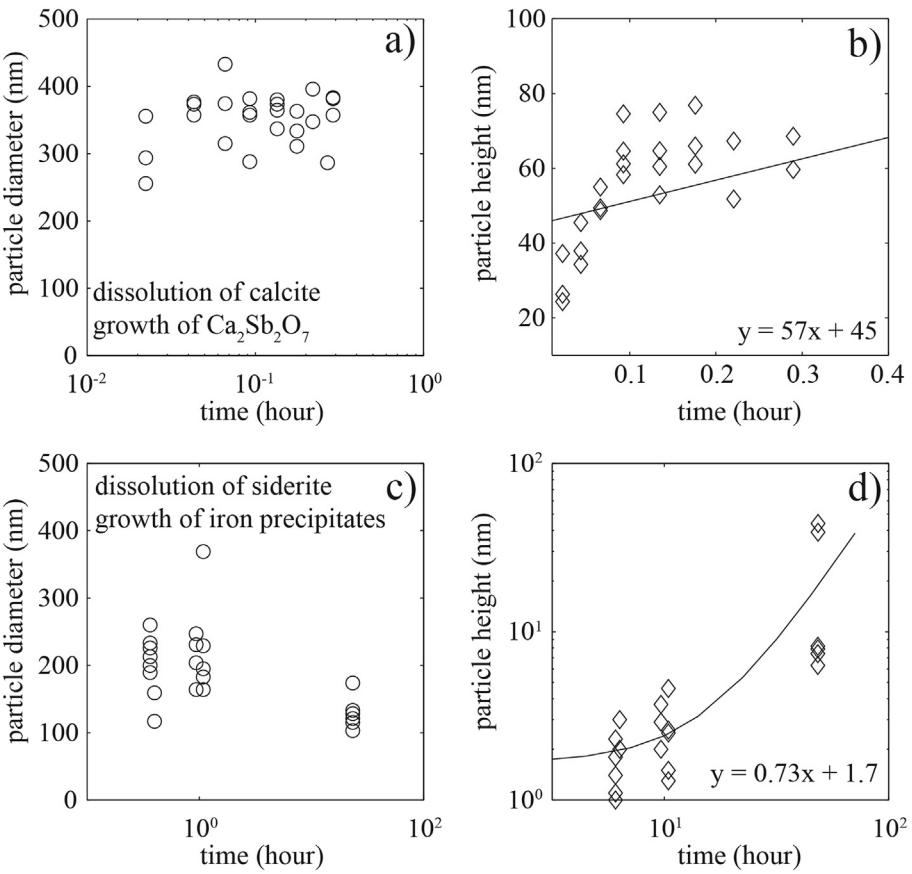

Figure 4. Measured *in-situ* kinetics of precipitate growth during coupled dissolution-precipitation over two carbonate surfaces. (a and b) Growth of an antimony precipitate on calcite (Fig. 3c and d) where the diameter of the particles (a) remains constant, while the height of the particles (b) increases with time at a rate of 57 nm h^{-1} (0.016 nm s^{-1}). (c and d) Growth of an oxyhydroxide precipitate on siderite (Fig. 3f) where the diameter of the particles (c) remains constant, while the height of the particles (d) increases with time at a rate of 0.73 nm h^{-1} (0.0002 nm s^{-1}). For both data sets a linear fit of the height growth is provided and the slope of this fit is used for the growth rate. On each plot, every symbol corresponds to one particle for which the error in the measurement using the AFM is well below the size of the symbol.

Please cite this article in press as: Renard, F., et al., Timescales of interface-coupled dissolution-precipitation reactions on carbonates, Geoscience Frontiers (2018), https://doi.org/10.1016/j.gsf.2018.02.013

Calcium-arsenate precipitate and calcite. In the presence of a high concentration of $As^{(V)}$ (500 ppm), precipitates are observed forming at the calcite surface at pH 11 (Fig. 3e). Immediately on contact of the surface with the undersaturated solution, tiny ~50 nm, initially scarce, particles nucleate at the calcite surface, more or less randomly, and without any observable preferred orientation (Renard et al., 2015). They cover a significant portion of the calcite surface within half an hour. Precipitated particles are generally too small to be easily identified; however both Raman data and thermodynamic simulations using PHREEQC show that these precipitates are consistent with hydrated Ca-arsenate phases such as pharmacolite ($CaHAsO_4 \cdot 2H_2O$) and johnbaumite ($Ca_5(AsO_4)_3OH$). The total reaction to produce pharmacolite can be written:

$$CaCO_3 + HAsO_4^{2-} + 2H_2O \leftrightarrow CaHAsO_4 \cdot 2H_2O + CO_3^{2-}$$

Calcium-antimony precipitate and calcite. In the presence of antimony, the precipitates are composed of oxycalcioroméite ($Ca_2Sb_2O_7$) and have an initial average height of a few nanometers, just within the limits of AFM recognition under the given fluid conditions and contact mode (Table 1). They grow initially as flat disks at the calcite surface until crystal facets can be observed (Renard et al., 2018). Precipitates are often located at kink sites on the calcite surface (Fig. 3d). They nucleate as individual particles with a rounded shape and then either pile up or aggregate to form larger particle clusters. They grow in size into larger, rounded, structured aggregates until they cover the entire calcite surface. The shape and size of these precipitates can be measured when their diameter is larger than 50 nm, the spatial resolution of the AFM technique used here. With time (within the time of the AFM experiment), the precipitates show a maximum diameter that remains more or less constant within the range 300–800 nm (Fig. 4a). The height of the precipitates is initially around 10 nm, before they tend to grow in height at a rate on the order of 0.016 nm s^{-1} (Fig. 4b). These observations are seen for acidic fluids in the presence of antimony; the lower the pH, the faster the calcite dissolved and more particles precipitated. The total reaction to produce the precipitates can be written as:

$$2CaCO_3 + 2Sb(OH)_6^- \leftrightarrow Ca_2Sb_2O_7 + 2CO_3^{2-} + 5H_2O + 2H^+$$

Calcium phosphate precipitates and calcite. When undersaturated solutions containing PO_4 ions pass over a calcite surface, the surface initially dissolves and then within minutes a precipitate begins to form, appearing as small (few nanometers) particles over the calcite surface and associated with the dissolving etch pit edges (Fig. 3i). In time these particles merge together along known crystallographic directions of step edges on the calcite {10–14} cleavage surface (see Video S1 for a film of this AFM reaction, reported in Klasa et al., 2013). Eventually after several hours the surface seems to be effectively covered with the merged particles, which have been identified as an amorphous Ca-phosphate phase. After a couple of days, characteristic peaks for apatite are seen in Raman spectroscopy (Wang et al., 2012a, b). Rather than passivating the calcite surface, it is known that apatite replaces calcite pseudomorphically so that a parent crystal of calcite is replaced by an apatite crystal that inherits the crystallographic characteristics of the parent. Similarly Carrara marble has been replaced by apatite in an interface-coupled dissolution-precipitation process (Pedrosa et al., 2015). Because the amorphous Ca-P phase could not be identified, a global reaction cannot be written for this system.

Supplementary data related to this article can be found at https://doi.org/10.1016/j.gsf.2018.02.013.

Iron oxide precipitates and siderite. At the siderite surface after contact with water, nucleated particles have an initial height of 1–2 nm after 1 min reaction and then grow with time into aggregate precipitates 130–220 nm wide and up to 80 nm high after 24 h of reaction. These particles are iron oxyhydroxides, likely goethite and/or ferrihydrite that are stable under the experimental conditions (Renard et al., 2017). The particles grow sideways in diameter until they reach a size in the range 130–220 nm (Fig. 4c), and then grow in height to 10–80 nm. With time, their height tends to increase and a linear fit provides a growth velocity of 0.0002 nm s^{-1} (Fig. 4d), in the range measured by Weidler et al. (1998) for the growth of goethite, although at different supersaturation. The siderite coupled dissolution-precipitation process can be described by five successive steps: (1) the release of Fe^{II} by siderite dissolution, (2) the formation of a $(Fe^{II}OH)^+$ complex, (3) the reaction of this complex with oxygen present in the fluid, (4) the formation of an aqueous complex $(Fe^{III}(OH^-)_3)^0$, and (5) the precipitation of solid $Fe^{III}(OH)_3$. Oxyhydroxides accumulate on the siderite surface with the next layers that nucleate and then grow sideways and upwards on top of the previous layers, decreasing the surface area available for further dissolution. A simplified global reaction can be written as:

$$Fe^{(II)}CO_3 + 3H_2O \leftrightarrow Fe^{(III)}(OH)_3 + CO_3^{2-} + 3H^+ + 1e^-$$

Hydrated magnesium carbonate precipitates and dolomite. When pure water is passed over a dolomite {10–14} cleavage surface, dissolution begins, followed by precipitation of small nanometer-sized particles distributed over the dissolving surface (Urosevic et al., 2012). Dissolution of dolomite occurs by the high nucleation rate of rhombohedral etch pits that are an order of magnitude smaller than on a dissolving calcite surface. Precipitation appears to occur randomly over the surface. When the pH of the solution is lowered, dissolution occurs much faster coupled with faster precipitation (Fig. 3g) so that in a short time (minutes) the dolomite surface becomes covered with the newly precipitated particles. Outflow solutions show a Ca:Mg ratio >1, accounted for by the stoichiometric dissolution of dolomite followed by the precipitation of a Mg-carbonate phase. This new precipitate in time begins to dissolve so that a steady state of element release finally is approached after several days. The new precipitated phase has been identified as a hydrated magnesium carbonate, possibly nesquehonite, $Mg(HCO_3)(OH) \cdot 2H_2O$. The overall reaction can be written as:

$$2(Ca_{0.5}, Mg_{0.5})CO_3 + 3H_2O \leftrightarrow Mg(HCO_3)(OH) \cdot 2H_2O + Ca^{2+} + CO_3^{2-}$$

Magnesium carbonate precipitates and magnesite. As for the case of dolomite, magnesite dissolution also occurs by the nucleation and spreading of rhombohedral etch pits. Under acidic conditions (pH 2) the rate of etch pit spreading varied in the range 0.003–0.04 nm s^{-1} (King and Putnis, 2013). Dissolution was followed by the formation of small nanometer-sized particles (Fig. 3h) precipitating at the magnesite surface after several minutes. The exact composition of this new phase could not be determined. However, Raman peaks show the presence of a hydrated magnesite phase (nesquehonite, artinite). Assuming the formation of nesquehonite, the overall reaction can be written as:

$$MgCO_3 + 3H_2O \leftrightarrow Mg(HCO_3)(OH) \cdot 2H_2O$$

4. Discussion

Data of Figs. 2 and 3 are schematically synthetized in Fig. 1b where it is shown that precipitates nucleate and grow at the carbonate mineral surface, many of them being located at specific enhanced dissolution sites such as etch pits or kink sites. The AFM

technique can image such particles only if they are attached at the surface. The scanning AFM tip will tend to move any particles not firmly attached on the surface. As already mentioned, we cannot rule out that some nanoparticle precipitates may form as pre-nucleation "clusters" in the boundary layer and then attach to the carbonate surface. In most examples described here, nanoparticles are seen on the carbonate surface as soon as the solution contacts the surface and within seconds of image scanning.

Such reactions where fluids access the minerals in rocks through grain boundaries are common in the Earth (Putnis, 2009). Grain boundaries have been called micro-reactors as exchange of elements initially occurs here through coupled dissolution and precipitation (Etschmann et al., 2014). Because in all experiments the injected fluid is undersaturated with respect to the new precipitating phase, there is a domain near the carbonate surface that must become supersaturated with the new phase. This domain of different fluid composition is called a boundary layer. We consider here the following coupled phenomena: (1) the nucleation and growth of a precipitate at or near the carbonate surface in a boundary layer whose volume is small enough such that (2) diffusion time is small and (3) local supersaturation is maintained, although the latter is known to fluctuate and depends on dissolution and precipitation rates that vary spatially (Putnis et al., 2014; Briese et al., 2017).

4.1. Lateral diffusion at the carbonate surface and the localization of precipitates

Our experimental observations show that the first particles often nucleate and grow at specific sites of a carbonate surface such as etch pits and kink edges (Fig. 3a, c, d). Note that the appearance of the deposits at "kinks" usually occurs because the deposits pin the steps at those points and thus, inhibit dissolution locally as the steps dissolve around the deposit, hence the appearance of the finger-like morphology emanating from these pinned points (Fig. 3d). These observations indicate that at these locations precipitates are more prone to remain attached. We hypothesize that it could be due to (1) either a higher localized flux of ions released from the dissolving carbonate surface that drives a local supersaturation with respect to the precipitate, (2) or some other surface forces that stabilize the precipitates.

The question arises whether large enough lateral concentration gradients could be maintained along the surface to allow for the localized growth of precipitates. Given the AFM observations, we can assume that dissolution takes place locally, not homogeneously over the entire surface, so we want to know whether this results in high enough differences in concentration at different locations of the surface (dissolution site vs. midway between dissolution sites). If concentrations of released ions are large enough it would be likely for precipitation to take place mainly near sites of dissolution. We consider a single dissolution site of dimension R_{diss} (Fig. 5a and b), with concentration contours of the released cation. For simplicity we consider the case of calcite where the cation is Ca^{2+}. The same approach could be extended to magnesite (Mg^{2+}), dolomite (Ca^{2+} and Mg^{2+}) and siderite (Fe^{2+}) and the conclusions below would be the same. We consider diffusion in half a sphere of radius R_{diff} with a source of radius R_{diss} at its center. At equilibrium, a difference in concentration between the dissolution site and midway between two dissolution sites, Δc, exists outwards from the dissolution site (Fig. 5b). A constant flux of cation Q_0 ($mol \cdot s^{-1}$) is produced at the dissolution site, and the local rate of carbonate dissolution k ($mol \cdot m^{-2} \cdot s^{-1}$) is:

$$k = \frac{Q_0}{2\pi R_{diss}^2} \quad (1)$$

An analytical solution for diffusion into half a hollow sphere of radius R_{diff} with a constant flux at $0 < x < R_{diss}$ is given by Carslaw and Jaeger (1959, p. 231, Eq. (7)).

$$Q_0 = \frac{2\pi D \cdot \Delta c \cdot R_{diff} \cdot R_{diss}}{\left(R_{diff} - R_{diss}\right)} \quad (2)$$

where Δc is the difference in concentration of Ca^{2+} ($mol\ m^{-3}$) between two locations at distances $x = R_{diff}$ and $x = R_{diss} < R_{diff}$, and D is the coefficient of diffusion of Ca^{2+} into water ($m^2\ s^{-1}$). Combining Eqs. (1) and (2), one obtains a characteristic length scale l_c

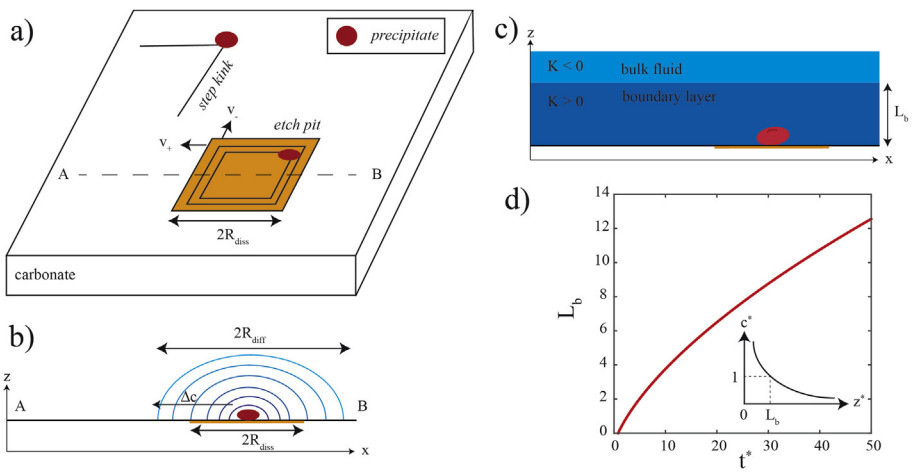

Figure 5. Sketch of an interface-coupled dissolution precipitation process in a boundary layer. (a) Carbonate mineral dissolves along rhombohedral etch pits and step edges. Dissolution products diffuse in the fluid and formation of precipitates occurs when a local supersaturation is reached. In several cases, precipitation occurs more favorably at locations where dissolution is kinetically favoured (etch pits, step edges). (b) Profile A–B where the decrease of concentration of the carbonate cation (Ca^{2+}, Mg^{2+}, Fe^{2+}) away from the precipitate is schematically represented, with a gradient of concentration Δc positive toward the center of the etch pit of half-size R_{diss}. During dissolution, these species diffuse over a diffusion length R_{diff}. (c) Sketch of the boundary layer of thickness L_b that separates two domains in the fluid where the reaction constant for the formation of the precipitates is positive in the boundary layer and negative in the bulk fluid. Note that in (b) and (c) the dimensions along the x-axis are larger than along the z-axis. On the carbonate surface step edges and steps in etch pits have sub-nanometer height (0.31 nm for calcite). (d) Maximum extent of the supersaturated boundary layer (non-dimensional $z^* = 1$, see inset) as a function of non-dimensional time t^* for the case without precipitation.

Please cite this article in press as: Renard, F., et al., Timescales of interface-coupled dissolution-precipitation reactions on carbonates, Geoscience Frontiers (2018), https://doi.org/10.1016/j.gsf.2018.02.013

$$l_c = \frac{R_{diss}\left(R_{diff} - R_{diss}\right)}{R_{diff}} = \frac{D \cdot \Delta c}{k} \quad (3)$$

To get a significant concentration difference, for example in the range $10^{-4} \leq \Delta c \leq 10^{-3}$ mol L^{-1} (i.e. 0.1–1 mol m^{-3}), and taking values $D = 2 \times 10^{-9}$ m^2 s^{-1} and k in the range 10^{-6} to 10^{-3} mol·m^{-2}·s^{-1} for the dissolution rate of calcite (Fig. 1 in Arvidson et al., 2003), this characteristic length scale falls in the range $0.03 \leq l_c \leq 40,000$ μm (Table 2). The largest values of l_c correspond to small dissolution rates and are larger than the size of the system studied here. For the smallest concentration difference and the largest dissolution rate, and if one considers a small value of the characteristic length scale on the order of $l_c = 200$ nm, one can calculate the diffusion radius from Eq. (3):

$$R_{diff} = \frac{R_{diss}^2}{R_{diss} - l_c} \quad (4)$$

The diffusion length is defined positive when $R_{diss} - l_c > 0$. For a typical etch pit side length on the order of $R_{diss} = 1$ μm (Figs. 2a and 3a), one obtains a diffusion length $R_{diff} = 1.25$ μm. For smaller dissolution rates, the diffusion length is diverging when l_c is approaching R_{diss}, indicating that an infinite distance would be required to get a significant concentration difference. Data of Table 2 show that in most cases $l_c > R_{diss}$ and, as a consequence, local dissolution cannot maintain a concentration gradient large enough to favour nucleation near the nucleation sites relative to other areas on the surface. That a range of dissolution rates exists at the surface of a mineral or a rock has been proposed in recent studies (Arvidson et al., 2003; Fischer et al., 2012; Emmanuel, 2014; Briese et al., 2017), resulting in a spectrum of dissolution rates. An interpretation is that dissolution can be much faster locally along steps and kinks (Fischer et al., 2014; Briese et al., 2017). We cannot rule out that this may happen in the present experiments and we test this hypothesis for the precipitates of Fig. 3a, c, which are localized inside etch pits.

For calcite, the average velocity of etch pit steps retreat, $v_{step} = \frac{v_{sum}}{2} = \frac{v_+ + v_-}{2}$ (Fig. 5a) has been measured for various solution compositions, under ambient conditions of temperature and partial pressure of CO_2, and was found to be in the range 2–6 nm s^{-1} for a range of pH between 5 and 10 (Ruiz-Agudo and Putnis, 2012). From the topography and dimensions of a typical etch pit on calcite (Figs. 2a and 3a, c), one can estimate the local dissolution rate k_{local} (mol m^{-2} s^{-1}). If $R_{diss} = 1$ μm is half the side length of an etch pit (Fig. 5a), $n_{step} = 10$ is the number of steps that dissolve simultaneously in this etch pit, $h_{step} = 3.1 \times 10^{-10}$ m is the height of each dissolving calcite step, and $V_{calc} = 31.2 \times 10^{-6}$ m^3 mol^{-1} is the molar volume of calcite, the local dissolution rate of calcite above an etch pit is:

$$k_{local} = \frac{n_{step} v_{step} h_{step}}{V_{calc} R_{diss}} \quad (5)$$

Taking $2 \times 10^{-9} \leq v_{step} \leq 6 \times 10^{-9}$ m s^{-1}, one obtains $2 \times 10^{-7} \leq k_{local} \leq 6 \times 10^{-7}$ mol m^{-2} s^{-1}, to be compared to the bulk dissolution rate at the same pH of the order of $10^{-6} \leq k \leq 10^{-5}$ mol m^{-2} s^{-1}. This difference of reaction rates was presented by Dove and Platt (1996) and is interpreted by the fact that higher bulk reaction rates could result from high energy surface features such as corners and rough and stepped surfaces (Briese et al., 2017), which are not imaged by AFM. This result allows us to conclude that local dissolution above an etch pit is rather slow in all experiments presented here and that a significant gradient of concentration Δc cannot be maintained along the dissolving surface. This indicates also that a high local dissolution rate cannot explain the localization of precipitates above etch pits or step edges (Fig. 3a, c, d) because diffusion is fast and tends to dissipate concentration gradient build-up during dissolution. An alternative explanation could be proposed: precipitates preferentially attach on these sites because the high surface energy associated with kinks or steps makes nucleation at these sites energetically favorable.

4.2. Transport and reaction in the boundary layer

We consider here a simplified geometry where dissolution occurs at the carbonate surface (Fig. 5c), providing a flux of species into the fluid above where the concentrations of species (both coming from the carbonate dissolution and those that are present initially in the surrounding fluid) are described by coupled equations that include a source term that accounts for the influx of species on one side, the diffusion of these species in the fluid, and a sink term that accounts for the precipitation of a new mineral if a local supersaturation is reached. We solve this system of coupled equations with relevant boundary conditions. The main goal then is to estimate the thickness L_b of a boundary layer in which precipitation occurs and the stability of this boundary layer over time.

For the limiting case of no precipitation, we consider diffusion into the semi-infinite space $0 \leq z \leq \infty$ with a constant flux k (mol·m^{-2}·s^{-1}) at $z = 0$, the fluid-mineral interface. The following set of equations describes dissolution and transport in the boundary layer. At $z = 0$,

$$k = -D \left.\frac{\partial c}{\partial z}\right|_{z=0} \quad (6)$$

Table 2
Characteristic length (l_c) and time (t_c) scales for interface-coupled dissolution-precipitation in the carbonate systems described in Table 1. For all systems, a diffusion coefficient $D = 2 \times 10^{-9}$ m^2 s^{-1} has been taken to calculate l_c and t_c. k: dissolution rate of the carbonate mineral. c_{eq}: equilibrium concentration of the precipitate.

Carbonate system	pH	c_{eq} (mol m^{-3})	k (mol m^{-2} s^{-1})	l_c (μm)	t_c (s)
Selenium + calcite	8.5–9.1	1[a]	10^{-6}–10^{-5}	200–2000	20–20,000
Arsenic + calcite	11.2	20[b]	10^{-6}–10^{-5}	4×10^3–4×10^4	8×10^3–8×10^5
Antimony + calcite	2.5–5.1	1.6×10^{-2}–4×10^{-1}[c]	10^{-5}–10^{-3}	0.03–80	<3.2
Phosphate + calcite	7.9	0.02–0.2[d]	10^{-6}–10^{-5}	4–400	<1–80
Siderite	1–1.6	2×10^{-2}–3×10^{-2}	1×10^{-7}–3×10^{-7}	40–200	9–180
Magnesite	2	0.96[e]	3×10^{-8}	64,000	2×10^6
Dolomite	3	0.96[e]	3.4×10^{-5}	56	1.6

[a] Solubility of Se-Ca hydrate (Fig. 4b, Nishimura et al., 2009) for Ca-Se precipitate.
[b] Solubility of pharmacolite (Rodríguez-Blanco et al., 2007) for Ca-As precipitate.
[c] Solubility of roméite (Cornelis et al., 2011) for Ca-Sb precipitate.
[d] Solubility of hydroxyapatites (Fulmer et al., 2002) for calcium-phosphate precipitate.
[e] Solubility of nesquehonite (Dong et al., 2008) for hydrated Mg-carbonate precipitate.

Please cite this article in press as: Renard, F., et al., Timescales of interface-coupled dissolution-precipitation reactions on carbonates, Geoscience Frontiers (2018), https://doi.org/10.1016/j.gsf.2018.02.013

and if one considers the dimensionless concentration $c^* = \frac{c}{c_{eq}}$ where c_{eq} is the concentration at equilibrium for the precipitating phase, the characteristic length scale $l_c = \frac{Dc_{eq}}{k}$, and the dimensionless distance $z^* = \frac{z}{l_c}$, then Eq. (6) becomes:

$$\left.\frac{\partial c^*}{\partial z^*}\right|_{z^*=0} = -1 \quad (7)$$

The diffusive transport in the boundary layer is described by:

$$\frac{\partial c}{\partial t} = -D\frac{\partial^2 c}{\partial z^2} \quad (8)$$

that can be transformed into the dimensionless form:

$$\frac{\partial c^*}{\partial t^*} = -\frac{\partial^2 c^*}{\partial z^{*2}} \quad (9)$$

where $t^* = \frac{t}{t_c}$ and using the characteristic time $t_c = \frac{Dc_{eq}^2}{k^2}$. The analytical solution for this equation is given by Carslaw and Jaeger (1959, p. 75, Eq. (8)).

$$c^*\left(z^*, t^*\right) = 2\sqrt{\frac{t^*}{\pi}}e^{z^{*2}/4t^*} - z^*\mathrm{erfc}\left(\frac{z^*}{2\sqrt{t^*}}\right) \quad (10)$$

The concentration at the mineral-water surface is given by:

$$c^*\left(0, t^*\right) = 2\sqrt{\frac{t^*}{\pi}} \quad (11)$$

and supersaturation is reached when $c > c_{eq}$, or $c^* > 1$ and this takes place when $t^* > \frac{\pi}{4}$, corresponding to $t = \frac{\pi}{4}t_c = \frac{\pi}{4}\frac{Dc_{eq}^2}{k^2}$, which depends on both the equilibrium concentration and the dissolution rate and therefore will vary among the carbonate minerals. Taking a typical value for the diffusion coefficient in water at 25 °C, $D = 2 \times 10^{-9}$ m^2 s^{-1}, k in the range of $10^{-6} - 10^{-3}$ mol m^{-2} s^{-1} for the dissolution rate of carbonate minerals, and equilibrium concentration in the range of $10^{-1} - 10^{3}$ mol m^{-3}, the characteristic length l_c varies in the range of $3 \times 10^{-8} - 4 \times 10^{-2}$ m and the characteristic time scale t_c varies in the range between less than one second to 2×10^6 s. This indicates that precipitates could form immediately in some systems, whereas when the equilibrium concentration to precipitate a new mineral is large or when the dissolution rate is small, the critical time to reach supersaturation will be large enough such that no precipitate will be observed after several hours in the AFM experiments.

By solving Eq. (10) numerically, it is shown that the concentration will always increase with time and distance from the mineral-surface. The consequence is that the thickness L_b of the boundary layer where supersaturation is maintained increases with time (Fig. 5d), without reaching a steady-state as long as the fluid is stagnant or if a constant concentration is imposed at some distance from the mineral surface. This is possible as long as there is an infinite water reservoir above the mineral surface. For the case where there is another mineral at a given distance or any other boundary with a fixed concentration, the value of L_b will be limited by such a boundary and the whole volume of water between the boundaries might become supersaturated as long as dissolution continues.

Since precipitates do form in the boundary layer, it is possible to add a sink term to Eq. (10). For precipitation close to the equilibrium concentration, where we can assume that the rate of precipitation has the form $k_p(c - c_{eq})$ where k_p is a measured precipitation rate (mol m^{-2} s^{-1}), the numerical solution of Eq. (10) shows that L_b will still increase with time, more slowly than if no precipitates formed, and will not reach a steady state. Similarly, if one adds the diffusion of a species A from the mineral surface to the boundary layer, and the diffusion of another species B from the bulk solution to the boundary layer and the formation of precipitates whose rate is given by $k_p(c_{AB} - c_{eq,AB})$, the thickness of the boundary layer will also increase with time, without reaching steady-state, although exceedingly slower for higher values of k_p.

These results are now applied for the various carbonate systems for which AFM experiments allow to measure the local dissolution rate and where precipitates are observed. The two characteristic parameters l_c and t_c control the time scale and thickness of the boundary layer, respectively. In Table 2, these two parameters are represented for the seven carbonate systems considered in the present study. We consider here that the precipitation of the new phase is slower than the dissolution of the carbonate, as it is observed with these systems. The characteristic time required to reach supersaturation on the surface can vary between less than a second for the calcite-antimony system to several hours for the calcite-arsenic system. Overall this approach indicate that in some cases precipitates will form faster in the experiments, and in other cases it will take several hours. However, in some cases precipitates are observed faster than predicted (for example for the calcite-arsenic system). This could be due to the initial formation of a phase with lower solubility than what is observed after 12 h, when Raman spectroscopy was used to identify it or to the lack of well-characterized solubility data for the hydrated phases in the calcium-arsenic system. For magnesite, which has a much lower dissolution rate, precipitates form much later than when compared to the dolomite case. For the smallest time scales below 1.5 min, the characteristic times are smaller than the time intervals used to scan the carbonate surface and precipitates form immediately upon injection of the fluid, which is observed in the experiments.

Note that here we have made the assumptions that the nucleation and precipitations of the new phase are slower than dissolution of the carbonate, and that the surface of the carbonate does not become passivated because of the accumulation of precipitates, although dissolution rates may decrease in time. In all systems, at the time required to reach supersaturation, the boundary layer reaches a characteristic thickness from sub-micrometer to several hundred of micrometers or even several millimeters for the arsenic-calcite system. In the case of reduction of the dissolution rate of the carbonate due to surface passivation, the characteristic length and time scales would increase.

The evolution of a mineral-fluid boundary layer is a dynamic process where ion concentrations will vary dependent on dissolution and precipitation rates. Using phase shift interferometry it has been shown that the composition of the boundary layer differs vastly from the bulk solution (Putnis et al., 2005; Ruiz-Agudo et al., 2016). Ion-specific and micro-pH electrodes have also shown the compositional variation within the boundary layer. Speciation within the boundary layer changes constantly and depends on the kinetics of mineral surface reactions. The boundary layer is a zone where ion associations and potential dynamic hydration relationships between ionic species may lead to the formation of ion clusters or pre-nucleation species. Stable pre-nucleation ion clusters of calcium carbonate have been shown to form even in undersaturated solutions (Gebauer et al., 2014 and references therein). This may explain the AFM observations where tiny (nm sized), probably amorphous, nano-particles of a new product phase "arrive" on the dissolving surfaces of the parent carbonates described here. This proposes a growth mechanism that differs from classical crystal growth theories traditionally described as ion by ion addition to active growth sites (Teng, 2013 and references

Please cite this article in press as: Renard, F., et al., Timescales of interface-coupled dissolution-precipitation reactions on carbonates, Geoscience Frontiers (2018), https://doi.org/10.1016/j.gsf.2018.02.013

therein). Recent molecular dynamics simulations have added significantly to our understanding of the potential stability of pre-nucleation phases (Demichelis et al., 2011; Wallace et al., 2013).

5. Conclusion

Series of experiments where dissolution of carbonates can be observed *in situ* under ambient conditions have demonstrated that when the cation present in the carbonate is released, it can bind with other chemical species and precipitate as new phases that grow in the form of nanoparticles. These phases are either hydrated minerals made of the same compounds as in the carbonate, or can trap species present in the water such as arsenic, selenium, antimony or phosphate. This so-called interface-coupled dissolution-precipitation process is controlled by the presence of a fluid boundary layer characterized by two non-dimensional numbers: a characteristic length scale and a characteristic formation time (see Table 2). This boundary layer does not reach an equilibrium thickness if the fluid above is static and its thickness grows continuously with time as dissolution of the carbonate proceeds. At the mineral surface, the new precipitates tend to attach at sites where the surface energy is higher (i.e. where the surface is rougher). In most cases, the carbonate surface does not have an initial control on the orientation of the new particles. These particles initially grow as flat platelets, up to 100–200 nm wide and several nanometers thick, that then grow in height to reach several tens of nanometers, a size where crystallographic facets can often be observed under the AFM.

This interface-coupled process that occurs in a micro-reactor, the boundary layer, controls many transformations of carbonate minerals in shallow Earth environments. It happens locally even if the fluid is undersaturated with respect to the new precipitates at the macroscopic scale. This phenomenon has important environmental implications for the trapping of pollutants (arsenic, selenium, antimony, phosphate) on calcite surfaces. It has also implications on how dissolved species are released into the pore fluids, as some of them will be trapped as new phases at the mineral surface, leading to the observations that the dissolution of carbonates could appear as an incongruent process at the macroscopic scale because some of the released species become trapped in the form of new minerals precipitated at the carbonate surface.

Acknowledgements

CVP acknowledges funding through the Marie Curie ITN Grant No. PITN-GA-2012-317235 (CO_2 React). The present study received funding from the European Union's Horizon 2020 Research and Innovation Programme under the ERC Advanced Grant Agreement No. 669972 (Disequilibrium Metamorphism) to AR.

References

Alexandratos, V.G., Elzinga, E.J., Reeder, R.J., 2007. Arsenate uptake by calcite: macroscopic and spectroscopic characterization of adsorption and incorporation mechanisms. Geochimica et Cosmochimica Acta 71, 4172–4187.

Arvidson, R.S., Ertan, I.E., Amonette, J.E., Luttge, A., 2003. Variation in calcite dissolution rates: a fundamental problem? Geochimica et Cosmochimica Acta 67 (9), 1623–1634.

Briese, L., Arvidson, R.S., Lüttge, A., 2017. The effect of crystal size variation on the rate of dissolution–A kinetic Monte Carlo study. Geochimica et Cosmochimica Acta 212, 167–175.

Carslaw, H.S., Jaeger, J.C., 1959. Conduction of Heat in Solids (vol. 1). Clarendon Press, Oxford.

Cornelis, G., Van Gerven, T., Snellings, R., Verbinnen, B., Elsen, J., Vandecasteele, C., 2011. Stability of pyrochlores in alkaline matrices: solubility of calcium antimonate. Applied Geochemistry 26 (5), 809–817.

Davis, K.J., Dove, P.M., De Yoreo, J.J., 2000. The role of Mg^{2+} as an impurity in calcite growth. Science 290, 1134–1137.

Demichelis, R., Raiteri, P., Gale, J.D., Quigley, D., Gebauer, D., 2011. Stable pre-nucleation mineral clusters are liquid-like ionic polymers. Nature Communications 2, 590.

Dong, M., Cheng, W., Li, Z., Demopoulos, G.P., 2008. Solubility and stability of nesquehonite ($MgCO_3 \cdot 3H_2O$) in NaCl, KCl, $MgCl_2$, and NH_4Cl solutions. Journal of Chemical & Engineering Data 53 (11), 2586–2593.

Dove, P.M., Hochella Jr., M.F., 1993. Calcite precipitation mechanisms and inhibition by orthophosphate: in situ observations by scanning force microscopy. Geochimica et Cosmochimica Acta 57, 705–714.

Dove, P.M., Platt, F.M., 1996. Compatible real-time rates of mineral dissolution by atomic force microscopy (AFM). Chemical Geology 127 (4), 331–338.

Emmanuel, S., 2014. Mechanisms influencing micron and nanometer-scale reaction rate patterns during dolostone dissolution. Chemical Geology 363, 262–269.

Etschmann, B., Brugger, J., Pearce, M.A., Ta, C., Brautigan, D., Jung, M., Pring, A., 2014. Grain boundaries as microreactors during reactive fluid flow: experimental dolomitization of a calcite marble. Contributions to Mineralogy and Petrology 168, 1045.

Fischer, C., Arvidson, R.S., Lüttge, A., 2012. How predictable are dissolution rates of crystalline material? Geochimica et Cosmochimica Acta 98, 177–185.

Fischer, C., Kurganskaya, I., Schäfer, T., Lüttge, A., 2014. Variability of crystal surface reactivity: what do we know? Applied Geochemistry 43, 132–157.

Fulmer, M.T., Ison, I.C., Hankermayer, C.R., Constantz, B.R., Ross, J., 2002. Measurements of the solubilities and dissolution rates of several hydroxyapatites. Biomaterials 23 (3), 751–755.

Gebauer, D., Kellermeier, M., Gale, J.D., Bergström, L., Cölfen, H., 2014. Pre-nucleation clusters as solute precursors in crystallization. Chemical Society Reviews 43, 2348–2371.

King, H.E., Putnis, C.V., 2013. Direct observations of the influence of solution composition on magnesite dissolution. Geochimica et Cosmochimica Acta 109, 113–126.

Klasa, J., Ruiz-Agudo, E., Wang, L.J., Putnis, C.V., Valsami-Jones, E., Menneken, M., Putnis, A., 2013. An atomic force microscopy study of the dissolution of calcite in the presence of phosphate ions. Geochimica et Cosmochimica Acta 117, 115–128.

Liu, Z., Deybrodt, W., 1997. Dissolution kinetics of calcium carbonate minerals in H_2O-CO_2 solutions in turbulent flow: the role of the diffusion boundary layer in the slow reaction $H_2O + CO_2 = H^+ + HCO_3^-$. Geochimica et Cosmochimica Acta 14, 2879–2889.

Liu, Z., Dreybrodt, V., 2001. Kinetics and rate-limiting mechanisms of dolomite dissolution at various CO_2 partial pressures. Science in China Series B Chemistry 44 (5), 500–509.

Montes-Hernandez, G., Concha-Lozano, N., Renard, F., Quirico, E., 2009. Removal of oxyanions from synthetic wastewater via carbonation process of calcium hydroxide: fundamentals and applications. Journal of Hazardous Materials 166, 788–795.

Morse, J.W., Arvidson, R.S., 2002. The dissolution of major sedimentary carbonate minerals. Earth Science Reviews 58, 51–84.

Morse, J.W., Arvidson, R.S., Lüttge, A., 2007. Calcium carbonate formation and dissolution. Chemistry Review 107 (2), 342–381.

Nishimura, T., Hata, R., Hasegawa, F., 2009. Chemistry of the M (M= Fe, Ca, Ba)-Se-H_2O systems at 25 °C. Molecules 14 (9), 3567–3588.

Paquette, J., Reeder, R.J., 1995. Relationship between surface structure, growth mechanism, and trace element incorporation in calcite. Geochimica et Cosmochimica Acta 59, 735–749.

Parkhurst, D.L., Appelo, C.A.J., 1999. Users Guide to PHREEQC (Version 2) a Computer Program for Speciation, Batch Reaction, One Dimensional Transport and Inverse Geochemical Calculations. Water-Resources Investigation report 99-4259. U.S. Geological Survey, Washington, DC, p. 312.

Pedrosa, E.T., Putnis, C.V., Putnis, A., 2015. The pseudomorphic replacement of marble by apatite: the role of fluid composition. Chemical Geology 425, 1–11.

Phillips-Lander, C.M., Parnell, S.R., McGraw, L.E., Madden, M.E., 2017. Carbonate dissolution rates in high salinity brines: implications for post-Noachian chemical weathering on Mars. Icarus. https://doi.org/10.1016/j.icarus.2017.10.024.

Pokrovsky, O.S., Golubev, S.V., Schott, J., Castillo, A., 2009. Calcite, dolomite and magnesite dissolution kinetics in aqueous solutions at acid to circumneutral pH, 25 to 150 °C and 1 to 55 atm pCO_2: new constraints on CO_2 sequestration in sedimentary basins. Chemical Geology 265, 20–32.

Putnis, A., 2002. Mineral replacement reactions: from macroscopic observations to microscopic mechanisms. Mineralogical Magazine 66 (5), 689–708.

Putnis, A., 2009. Mineral replacement reactions. In: Oelkers, E.H., Schott, J. (Eds.), Thermo- Dynamics and Kinetics of Water–rock Interaction. Reviews in Mineralogy & Geochemistry, vol. 30, pp. 87–124.

Putnis, C.V., Tsukamoto, K., Nishimura, Y., 2005. Direct observations of pseudomorphism: compositional and textural evolution at a fluid-solid interface. American Mineralogist 90, 1909–1912.

Putnis, C.V., Ruiz-Agudo, E., 2013. The mineral-water interface: where minerals react with the environment. Elements 9, 177–182.

Putnis, C.V., Renard, F., King, H.E., Montes-Hernandez, G., Ruiz-Agudo, E., 2013. Sequestration of selenium on calcite surfaces revealed by nanoscale imaging. Environmental Science & Technology 47 (23), 13469–13476.

Putnis, C.V., Ruiz-Agudo, E., Hövelmann, J., 2014. Coupled fluctuations in element release during dolomite dissolution. Mineralogical Magazine 78, 1–7.

Please cite this article in press as: Renard, F., et al., Timescales of interface-coupled dissolution-precipitation reactions on carbonates, Geoscience Frontiers (2018), https://doi.org/10.1016/j.gsf.2018.02.013

Renard, F., Putnis, C.V., Montes-Hernandez, G., Ruiz-Agudo, E., Hövelmann, J., Sarret, G., 2015. Interactions of arsenic with calcite surfaces revealed by in situ nanoscale imaging. Geochimica et Cosmochimica Acta 159, 61–79.

Renard, F., Putnis, C.V., Montes-Hernandez, G., King, H.E., 2017. Siderite dissolution coupled to iron oxyhydroxide precipitation in the presence of arsenic revealed by nanoscale imaging. Chemical Geology 449, 123–134.

Renard, F., Putnis, C.V., Montes-Hernandez, G., King, H.E., Breedveld, G.D., Okkenhaug, G., 2018. Sequestration of antimony on calcite observed by time-resolved nanoscale imaging. Environmental Science & Technology 52, 107–113.

Rodríguez-Blanco, J.D., Jiménez, A., Prieto, M., 2007. Oriented overgrowth of pharmacolite ($CaHAsO_4 \cdot 2H_2O$) on gypsum ($CaSO_4 \cdot 2H_2O$). Crystal Growth & Design 7 (12), 2756–2763.

Rimstidt, J.D., Balog, A., Webb, J., 1998. Distribution of trace elements between carbonate minerals and aqueous solutions. Geochimica et Cosmochimica Acta 62 (11), 1851–1863.

Ruiz-Agudo, E., Putnis, C.V., 2012. Direct observations of mineral fluid reactions using atomic force microscopy: the specific example of calcite. Mineralogical Magazine 76 (1), 227–253.

Ruiz-Agudo, E., Putnis, C.V., Putnis, A., 2014. Coupled dissolution and precipitation at mineral–fluid interfaces. Chemical Geology 383, 132–146.

Ruiz-Agudo, E., King, H.E., Patiño-López, L.D., Putnis, C.V., Geisler, T., Rodriguez-Navarro, C., Putnis, A., 2016. Control of silicate weathering by interface-coupled dissolution-precipitation processes at the mineral-solution interface. Geology 44, 567–570.

Stipp, S.L.S., Christensen, J.T., Lakshtanov, L.Z., Baker, J.A., Waight, T., 2006. Rare Earth element (REE) incorporation in natural calcite: upper limits for actinide uptake in a secondary phase. Radiochimica Acta 94, 523–528.

Teng, H.H., 2013. How ions and molecules organize to form crystals. Elements 9, 189–194.

Urosevic, M., Rodriguez-Navarro, C., Putnis, C.V., Cardell, C., Putnis, A., Ruiz-Agudo, E., 2012. In situ nanoscale observations of the dissolution of (10–14) dolomite cleavage surfaces. Geochimica et Cosmochimica Acta 80, 1–13.

Wallace, A., Hedges, L.O., Fernandez-Martinez, A., Raiteri, P., Gale, J.D., Waychunas, G.A., Whitelam, S., Banfield, J.F., De Yoreo, J.J., 2013. Microscopic evidence for liquid-liquid separation in supersaturated $CaCO_3$ solutions. Science 341, 885–889.

Wang, L.J., Ruiz-Agudo, E., Putnis, C.V., Menneken, M., Putnis, A., 2012a. Kinetics of calcium phosphate nucleation and growth on calcite: implications for predicting the fate of dissolved phosphate species in alkaline soils. Environmental Science & Technology 46, 834–842.

Wang, L., Li, S., Ruiz-Agudo, E., Putnis, C.V., Putnis, A., 2012b. Posner's clusters revisited: direct imaging of nucleation and growth of nanoscale calcium phosphate clusters at the calcite-water interface. CrystEngComm 14, 6252–6256.

Weidler, P.G., Hug, S.J., Wetche, T.P., Hiemstra, T., 1998. Determination of growth rates of (100) and (110) faces of synthetic goethite by scanning force microscopy. Geochimica et Cosmochimica Acta 62 (21), 3407–3412.

Please cite this article in press as: Renard, F., et al., Timescales of interface-coupled dissolution-precipitation reactions on carbonates, Geoscience Frontiers (2018), https://doi.org/10.1016/j.gsf.2018.02.013